ADVANCED FUNCTIONAL MATERIALS
www.afm-journal.de

Rational Design of 3D Space Connected Donor–Acceptor System in Covalent Organic Frameworks for Enhanced Photocatalytic Performance

Yinghui Xie, Fengyi Mao, Qiuyu Rong, Xiaolu Liu, Mengjie Hao, Zhongshan Chen, Hui Yang, Geoffrey I. N. Waterhouse, Shengqian Ma,* and Xiangke Wang**

Herein, a rational strategy is presented to reduce the energy barrier of singlet ground state to singlet excited state transitions, whilst simultaneously reducing energy losses in populating triplet excited states. The approach relies on constructing 3D space connected donor–acceptor systems in COFs. The 3D space connected D–A system in 8-connected 3D COFs (denoted as COF-1 and COF-2) allows the efficient transfer of electrons, overcoming the traditional electron transport limitations of 2D COFs and significantly boosting the solar energy utilization efficiency under visible light irradiation. COF-2, possessing an extended π-conjugated structure relative to COF-1, demonstrated high selectivity for the photocatalytic generation of H_2O_2 (6.93 mmol g^{-1} h^{-1}) in natural seawater without the need for sacrificial reagents, exceeding the performance of most previously reported COF-based photocatalysts. The 3D space connected D–A system reported in this work offers a new approach for optimizing electron and energy transfer in COF-based photocatalysts for H_2O_2 production and other applications.

1. Introduction

As a new generation of organic porous crystal materials, covalent organic frameworks (COFs) receive considerable attention owing to their well-defined structure, high porosity, good stability, low skeleton density, and customizable functionality.[1] These features make them ideal candidate for use in separation,[2] sensing,[3] catalysis,[4] photoluminescence,[5] energy storage,[6] and environmental remediation.[7] Recently, COFs, particularly 2D COFs, have found applications in photocatalysis, based on their small electronic bandgaps, effective exciton migration, and fast photogenerated charge separation.[8] However, the rapid charge (electron–hole) recombination, energy losses during charge excitation and migration, and operational instability hamper the photocatalytic activity of COFs. Furthermore, effective separation of photogenerated charges generally relies on the use of sacrificial reagents, which hinders the practical applications of COFs-based photocatalysts.[9] Generally, electrons are excited from the ground state (S_0) to the lowest singlet excited state (S_1) or higher singlet excited state (S_2, S_3, ...S_n) in COFs under visible light irradiation, thus creating charges to drive photocatalytic processes (**Figure 1a,b**).[10] Afterward, most of the singlet excited state (S_1, S_2, ...S_n) electrons quickly decays back to S_0 through fluorescence emission, which reduces the charge carrier utilization efficiency. A portion of the electrons in S_n (n = 1, 2, 3, etc.) may also migrates to the lowest triplet excited state (T_1) through the intersystem crossing (ISC) processes, which decreases electron–hole combination kinetics and energy losses.[11] These excited electrons in the T_1 state can catalyze reactant conversion or convert O_2 to $^1O_2$, driving nonradiative processes such as electron transfer, energy transfer, and atom transfer in photocatalysis. Since, the $T_1 \rightarrow S_0$ transition is spin-forbidden, the charge carrier lifetime of T_1 electrons can be very long.[12] Minimizing the energy gap (ΔE_{ST}) between S_1 and T_1 levels and enhancing the ISC efficiency is therefore a promising way to reduce the energy losses during photocatalysis (Figure 1b).

Recently, researchers have made great efforts to improve the electron utilization efficiency and charge transfer properties of COF-based photocatalysts, using approaches such as introducing photosensitizers,[13] building donor–acceptor (D–A units),[14] designing D–π–A units,[9] optimizing bandgap energies,[15] tuning excited state electronic structures and charge transport,[10a,16] constructing molecular heterojunctions,[17] amongst others.[18] Most of these studies have focused on the development of 2D COFs for photocatalytic applications. Compared with 2D structures, 3D frameworks are expected to offer advantages in that the photosensitive units should be able to more rapidly transfer

Y. Xie, F. Mao, Q. Rong, X. Liu, M. Hao, Z. Chen, H. Yang, X. Wang
College of Environmental Science and Engineering
North China Electric Power University
Beijing 102206, P. R. China
E-mail: h.yang@ncepu.edu.cn; xkwang@ncepu.edu.cn

G. I. N. Waterhouse
School of Chemical Sciences
The University of Auckland
Auckland 1142, New Zealand

S. Ma
Department of Chemistry
University of North Texas
Denton, TX 76201, USA
E-mail: shengqian.ma@unt.edu

The ORCID identification number(s) for the author(s) of this article can be found under https://doi.org/10.1002/adfm.202411077

DOI: 10.1002/adfm.202411077

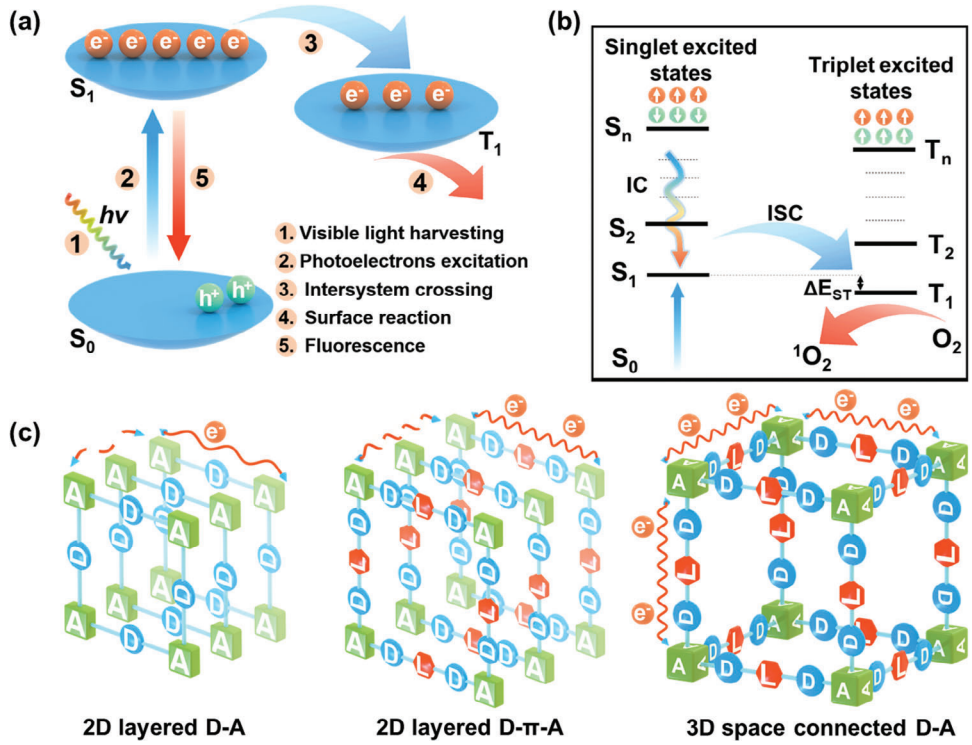

Figure 1. a) Schematic illustration of the light harvesting and energy transfer processes involved in triplet excited state-driven photocatalysis. b) Schematic illustration of energy levels and electron transfer pathways. c) Schematic illustration of a traditional donor–acceptor system in 2D COFs, and the 3D space connected D-A system in 3D COFs.

electrons to electron-deficient acceptors or alternatively accept electrons from electron-rich donors, thus achieving high photocatalytic activity.[19] However, it is a challenge to construct 3D COF photocatalysts with high connectivity while ensuring their spatial structure and photocatalytic performance (Figure 1c).[19a,b,20]

Hydrogen peroxide (H_2O_2), as a strong oxidant, bleach, and bactericide, is widely used in the chemical and paper industries, energy sector and environmental remediation.[21] The traditional anthraquinone method used industrially to produce H_2O_2 has many drawbacks, such as high energy consumption, high capital cost, and the generation of harmful waste.[22] Single-step photocatalytic production of H_2O_2 using oxygen dissolved in water provides a green, environmental friendly and sustainable method toward H_2O_2. In recent years, photocatalysts such as graphitic carbon nitride (g-C_3N_4), metal oxides, resins, COFs, conjugated polymers, and metal–organic frameworks (MOFs) have been explored for H_2O_2 production.[23] However, most of these photocatalysts require the use of sacrificial oxidants, which hinders their widespread practical application. With a view toward improving process economics, H_2O_2 production from seawater is very promising.[24] However, developing photocatalytic technologies for hydrogen peroxide production from seawater remains a huge challenge because corrosion and biofouling issues can damage the photocatalyst under practical conditions, reducing its activity and lifetime. 2D COFs can address many of these issues relating to photocatalytic synthesis of H_2O_2, but performance needs to be improved.[13b,14b,17a,25] Compared to 2D COFs, photosensitive units in 3D COFs can more quickly transfer electrons to electron-deficient acceptors or accept electrons from electron-rich donors.

To achieve the aforementioned objective, we herein designed and synthesized two 8-connected 3D COFs with the bcu topology via a [8 + 2] construction approach. The (2r,3s,5s,6s)-2,3,5,6-tetrakis(3,6-bis(4-formylphenyl)-9H-carbazol-9-yl) terephthalonitrile (4CzTFPN) linker served as both donor and acceptor. Compared to 2D D-A structures, such a 3D space connected D-A system spatially separated the highest occupied molecular orbitals (HOMO) and lowest unoccupied molecular orbitals (LUMO), thus overcoming the limitations of electron transport in 2D space and reducing the charge transfer energy losses from the S_0 to S_n (n = 1, 2, 3, etc.) levels and subsequently the S_n to T_1 levels through the high connectivity of the 3D frameworks (Figures 1c and 2a). Moreover, the planar conjugated structure of the benzene (denoted as COF-1) and naphthyl linkers (denoted as COF-2), together with the continuous delocalization channels, afforded highly extended π-conjugated systems. These systems enhance the photocatalytic activity of COFs and deliver high efficiency and selectivity for photocatalytic H_2O_2 production in natural seawater (4.42 and 6.93 mmol g^{-1} h^{-1} for COF-1 and COF-2, respectively) without the need for sacrificial reagents. The solar-chemical conversion efficiency of H_2O_2 production was determined to be 0.26% for COF-2, which far exceeds the solar-to-biomass efficiency by plants (global average 0.10%). These results serve as a valuable platform for the construction of 3D COF photocatalysts for various photocatalytic applications.

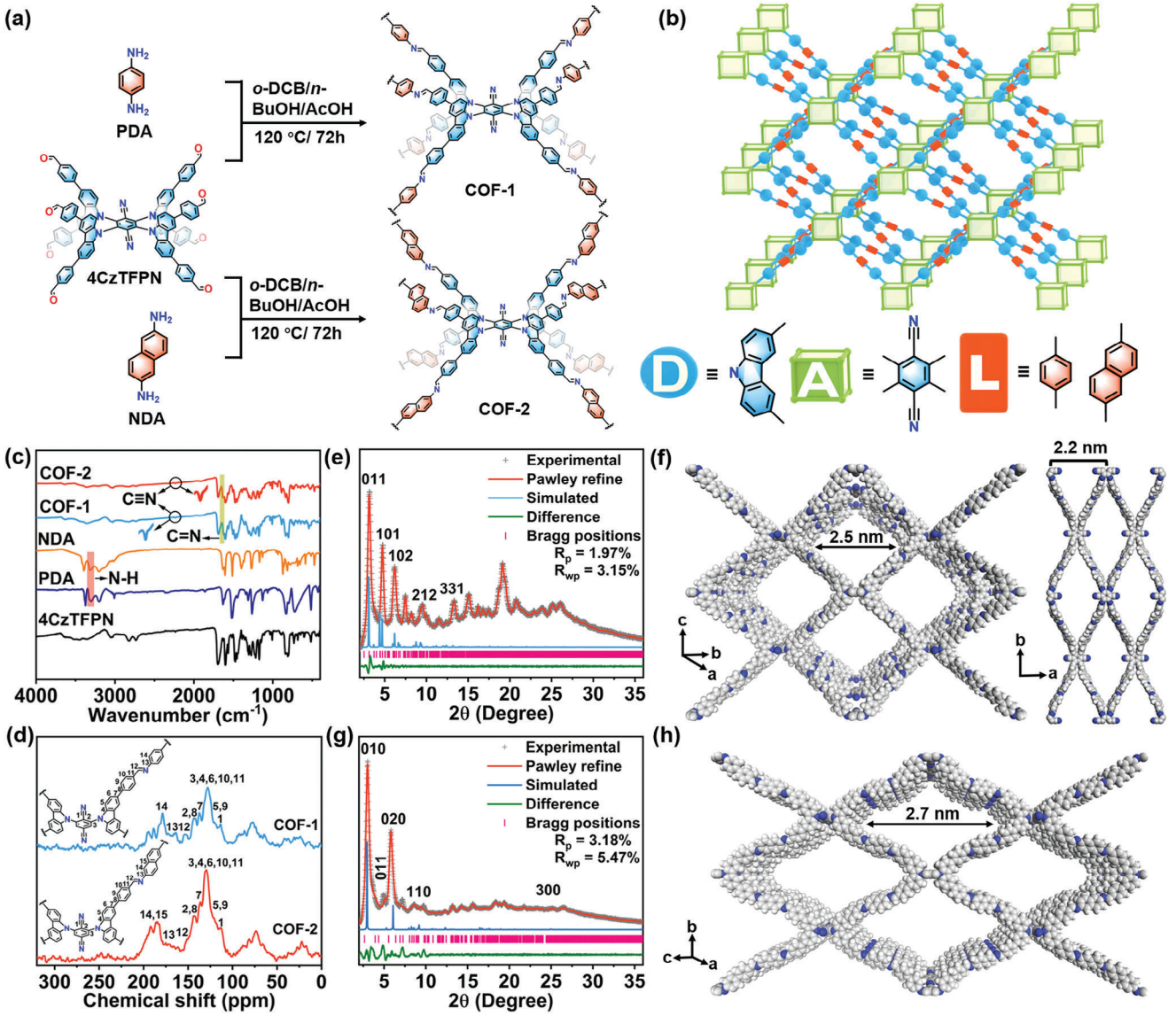

Figure 2. a) Illustration of the synthesis of 3D COFs. b) Topology representation of the bcu topology in 3D COF-1 and COF-2. c) FT-IR spectra for 4CzTFPN, PDA, NDA, COF-1, and COF-2. d) Solid-state ^{13}C CP/MAS NMR spectra of COF-1 and COF-2. e) Experimental PXRD patterns of COF-1 with corresponding Pawley refinement (red), simulated results (blue), and Bragg positions (pink) showing good fit to the experimental data (gray) with minimal differences (olive green). f) Crystal structure of COF-1. g) Experimental PXRD patterns of COF-2 with corresponding Pawley refinement (red), simulated results (blue), and Bragg positions (pink) showing good fit to the experimental data (gray) with minimal differences (olive green). h) Crystal structure of COF-2.

2. Results and Discussion

2.1. Synthesis and Characterization

As illustrated in Figure 2a,b, 8-connected aldehyde monomer (2r,3s,5s,6s)-2,3,5,6-tetrakis(3,6-bis(4-formylphenyl)-9H-carbazol-9-yl) terephthalonitrile (4CzTFPN) was reacted with liner linkers p-phenylenediamine (PDA) and 2,6-diaminonaphthalene (NDA) to synthesize the COF-1 and COF-2, respectively. Both COF-1 and COF-2 were obtained via an imine condensation with acetic acid as the catalyst in a mixture of 1,2-dichlorobenzene (*o*-DCB)/*n*-butanol (*n*-BuOH) at 120 °C for 3 days. Fourier transform infrared (FT-IR) spectroscopy and ^{13}C solid-state nuclear magnetic resonance (^{13}C ssNMR) spectroscopy were used to confirm the chemical structures of COF-1 and COF-2. The appearance of a strong FT-IR bands at ≈1625 cm^{-1} in both COFs verified the formation of imine C═N bonds in the frameworks (Figure 2c).[26] Moreover, the -CHO signals at ≈1689 cm^{-1} and -NH_2 signals at ≈3321 cm^{-1} characteristic of the reagents disappeared, further confirming the successful condensation reaction between the starting materials (Figure 2c). The presence of a C≡N stretching peak at 2233 cm^{-1} verified the existence of cyano groups in both COF-1 and COF-2. The ^{13}C ssNMR spectra of COF-1 and COF-2 showed peaks at

152 ppm, verifying the formation of imine groups, with additional peaks at ≈114 ppm attributed to the C≡N group of the 4CzTFPN linkers (Figure 2d).[27] The peaks at ≈165, 181, and 192 ppm in COF-2 are assigned to the carbon atoms on naphthalene rings (Figure 2d).

Next, we performed powder X-ray diffraction (PXRD) measurements and structural simulations to determine the 3D crystal structures of COF-1 and COF-2. The diffraction pattern of COF-1 showed peaks of 2θ angles ≈3.2°, 4.7°, 6.2°, 9.5°, and 13.3°, which were assigned to the (011), (101), (102), (212), and (331) planes, respectively (Figure 2e). The raw unit cell determined by Pawley refinement was suggested a PMM2 space group with parameters of a = 22.2169 Å, b = 48.0347 Å; c = 35.5372 Å, $\alpha = \beta = \gamma = 90°$ for COF-1 (Table S1, Supporting Information). The refined patterns based on the simulated structures of COF-1 revealed good consistency with the experimentally measured PXRD pattern (R_{wp} = 3.15%, R_p = 1.97%). Each 4CzTFPN linker in COF-1 bonds eight PDA linkers, forming an 8-connected open framework with the bcu topology (Figure 2b). The pore size is ≈2.5 nm (Figure 2f). The crystalline structure of COF-2 was also determined using experimental PXRD data, structure modeling, and Pawley refinement (Figure 2g,h). The results revealed that COF-2 crystalized in an IMM2 space group with unit cell parameters of a = 10.5634 Å, b = 32.7451 Å; c = 60.4926 Å, $\alpha = \beta = \gamma = 90°$ with R_{wp} = 5.47%, R_p = 3.18%. Results confirmed that COF-2 possessed high crystallinity and the same topology as COF-1 (Figure 2b; Table S2, Supporting Information). Scanning electron microscopy (SEM) images showed that COF-1 and COF-2 crystallized with a lamellar nanosheet morphology (Figure S1, Supporting Information). The high-resolution transmission electron microscopy (HRTEM) image of COF-1 revealed lattice fringes with a spacing ≈2.2 nm, close to the window size viewed along the c direction (Figure 2f; Figure S2, Supporting Information). Honeycomb-like porous structures were observed for COF-2, which is in accordance with the structural model viewed along the a/c direction (Figures 2h and 3a). These structures demonstrate an ordered alignment with high degrees of crystallinity. These data suggested the successful construction of 3D COF-1 and COF-2 with the desired structures.

The porosity of COF-1 and COF-2 were determined by measuring nitrogen sorption isotherms on fully activated samples at 77 K. The adsorption–desorption isotherms displayed type IV curves, indicating the presence of mesopore in both structures (Figure 3b). The Brunauer–Emmett–Teller (BET) surface areas were calculated to be 489.2 and 868.8 $m^2 g^{-1}$ for COF-1 and COF-2, respectively. Density functional theory (DFT) pore distribution analysis showed that the average pore diameters were 2.5 and 2.7 nm, respectively, in good general agreement with the predicted apertures in the simulated structures (Figure 3c). Thermal gravimetric analysis (TGA) revealed that both COF-1 and COF-2 were stable up to ≈400 °C under a N_2 atmosphere, suggesting good thermal stability (Figure S3, Supporting Information). We next examined the chemical stability of COF-1 and COF-2 by soaking the samples in organic solvents, natural seawater, HNO_3 (pH 1), or NaOH (pH 13) solutions. PXRD patterns revealed that the 3D frameworks retained their crystalline structures after 24 h treatment under all tested conditions (Figure S4, Supporting Information).

2.2. Photophysical and Electrochemical Properties

We then systematically tested the photophysical and electrochemical properties of COF-1 and COF-2. The UV–vis diffuse reflectance spectra (UV–vis DRS) for both COFs showed intense absorption over a wide wavelength range (200–800 nm), indicating their strong visible light harvesting ability (Figure 3d). COF-1 and COF-2 each have two absorption edges. The orange-red COF-1 showed two absorption edges at 568 and 637 nm, and corresponding optical bandgap energies calculated from Kubelka–Munk function transformed spectra were 2.41 and 2.03 eV, respectively. The reddish-brown COF-2 absorption edges at 576 and 642 nm, corresponding to bandgaps at 2.38 and 2.05 eV, respectively. (Figure 3d). Next, Mott–Schottky tests were carried out to estimate the conduction band (CB) positions of COF-1 and COF-2, which were determined to be −0.82 and −0.37 V versus normal hydrogen electrode (NHE), respectively (Figure S5, Supporting Information, equal to −1.02 and −0.57 V vs Ag/AgCl). The valence band (VB) positions were calculated as 1.15 and 1.53 eV for COF-1, 1.62 and 1.95 eV for COF-2, respectively, as determined from X-ray photoelectron spectroscopy valence band spectra (Figure S6, Supporting Information). Figure 3e compares the energy levels of the two COFs, as well as selected redox couples relevant to the current study: $O_2/{\cdot}O_2^-$ (−0.33 V vs NHE), and O_2/H_2O_2 (+0.68 V vs NHE).[25a,28] It suggests that suitable bandgap structures of both COF-1 and COF-2 are suitable for photoelectron transfer to support the photocatalytic reduction of O_2 to H_2O_2. Electrochemical impedance spectroscopy (EIS) was carried out to probe the electronic conductivity of COF-1 and COF-2. Compared to COF-1, COF-2 exhibited a relatively smaller semicircle radius in the Nyquist plot, implying a faster charge transfer rate and more efficient charge carrier separation ability (Figure 3f). COF-2 also exhibited a stronger photocurrent response than COF-1, indicating that it has a better charge separation efficiency due to the planar extended conjugation system of the naphthalene units in COF-2, which enhanced electron–hole separation (Figure 3g). Electron paramagnetic resonance (EPR) spectroscopy was used to investigate the light-induced charge carrier generation properties of COF-1 and COF-2. In contrast to spectra collected under dark conditions, both COF-1 and COF-2 showed strong signals at g = 2.003 under visible light, indicating that electrons were excited from the valence band to the conduction band (Figure 3h).[29] COF-2 showed a stronger EPR signal, consistent with better charge carrier generation efficiency. Time-resolved photoluminescence emission decay spectra (TRPL) showed that the average fluorescent lifetimes of COF-1 (0.86 ns) and COF-2 (0.85 ns) were approximately equal, while the PL intensity of COF-2 was lower than that of COF-1 (Figure 3i; Figure S7, Supporting Information). This suggested suppressed recombination of the photogenerated electron–hole pairs in COF-2. These results combined indicate that 3D COF-1 and COF-2 possessed high crystallinity, large porosity, good light harvesting ability, excellent electron conductivity, efficient charge separation, and transport properties, suggesting good potential for photocatalytic H_2O_2 production. As a proof of concept, we next conducted a series of photocatalytic experiments to evaluate the feasibility of 3D COFs for the synthesis of H_2O_2 from seawater. In particular, we aimed to investigate the effect of the 3D space-connected D–A system on the photocatalytic properties.

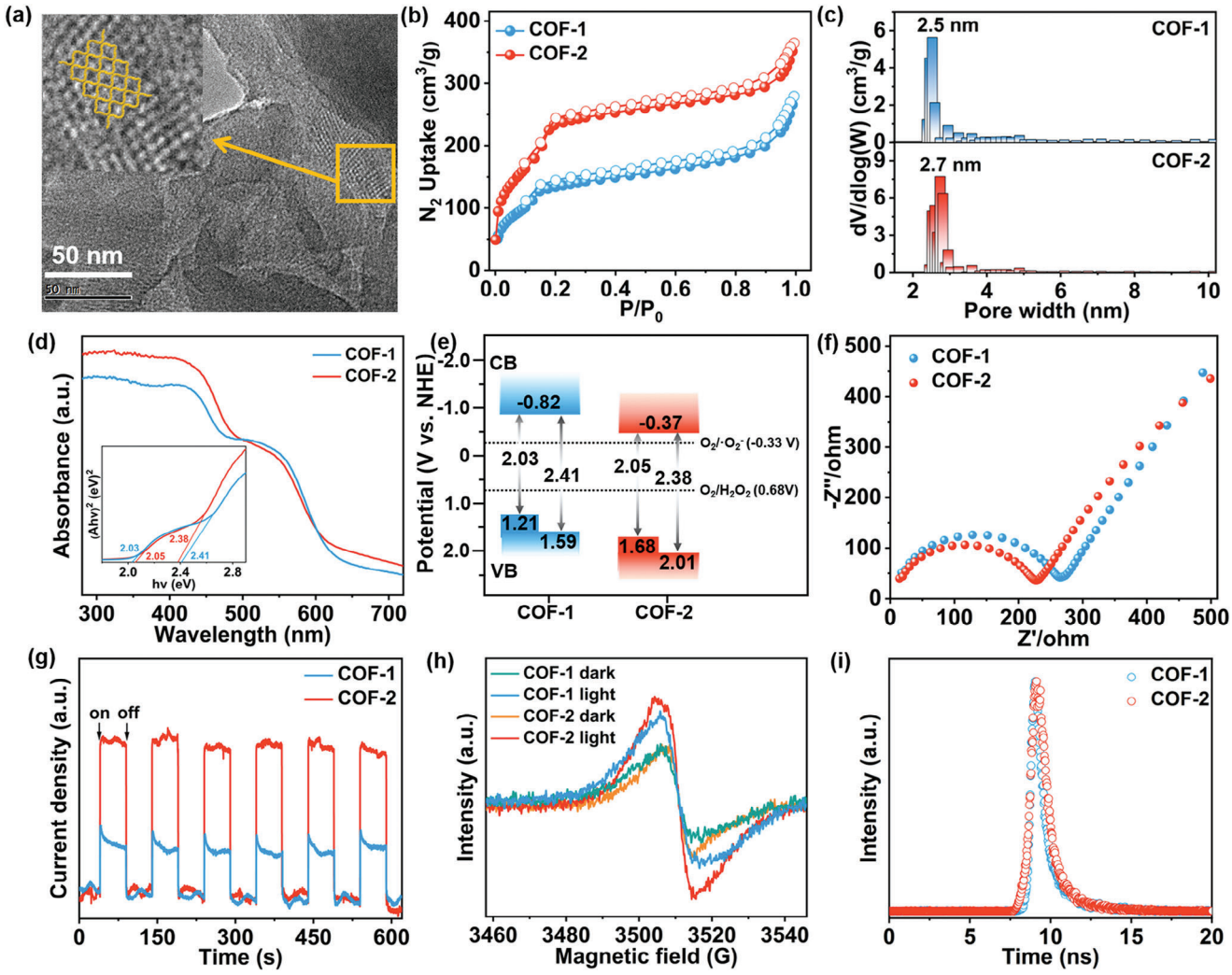

Figure 3. a) TEM image of COF-2 (insets highlight the honeycomb-like pores). b) N_2 adsorption–desorption isotherms measured at 77 K and c) corresponding pore size distributions for COF-1 and COF-2. d) UV–visible diffuse reflectance spectra for COF-1 and COF-2 (inset: Tauc plots for bandgap calculation). e) Band alignment of COF-1 and COF-2. f) Electrochemical impedance spectra (EIS) for COF-1 and COF-2. g) Photocurrent responses of COF-1 and COF-2. h) EPR spectra of COF-1 and COF-2 in the dark and under visible light irradiation. i) Time-resolved photoluminescence (TRPL) spectra of COF-1 and COF-2 (excitation at 375 nm).

2.3. Photocatalytic H_2O_2 Production Performance

The 3D COF-1 and COF-2 photocatalysts reported herein provide the opportunity to identify the key factors required for selective and efficient photocatalytic production of H_2O_2 from seawater thereby establishing a valuable structure-photocatalytic activity relationship. We first studied the photocatalytic H_2O_2 production performance of COF-1 and COF-2 in deionized water under visible light ($\lambda \geq 420$ nm) irradiation. No sacrificial agents were used. The corresponding H_2O_2 yield was detected by iodometry (Figure S8, Supporting Information).[30] The optimal photocatalyst dosage of 5 mg of COF in 50 mL of deionized water (solid/liquid ratio of 1/10, mg mL^{-1}) for each COF were determined and used for subsequent studies (Figure S9, Supporting Information). COF-2 displayed the significantly higher H_2O_2 production rate (7.86 mmol $h^{-1}g^{-1}$) than COF-1 (3.87 mmol h^{-1} g^{-1}) in deionized water (**Figure** 4a). After 120 min, the production capacities were 6.3 and 11.2 mmol g^{-1} for COF-1 and COF-2, respectively. The photocatalytic activity of COF-1 and COF-2 were further evaluated by conducting H_2O_2 production experiments in tap water (Figure 4b). COF-2 efficiently produced H_2O_2 in spiked tap water, with a production rate of 7.59 mmol $h^{-1}g^{-1}$. COF-1 showed relatively low activity under similar conditions (4.73 mmol h^{-1} g^{-1}). We next carried out experiments to determine the ability of COF-1 and COF-2 to produce H_2O_2 from natural seawater. The H_2O_2 production yields of COF-1 and COF-2 in seawater were 4.42 and 6.93 mmol h^{-1} g^{-1}, with the corresponding capacities being 7.80 and 11.0 mmol g^{-1} in 120 min, respectively (Figure 4c). The performance of both COFs in seawater was slightly lower than their performance in deionized water and tap water, which can be attributed to the high salinity of seawater. Marine microorganisms may also interfere with H_2O_2 formation or consume H_2O_2 in seawater. To our knowledge, the photocatalytic H_2O_2 production performance of COF-2

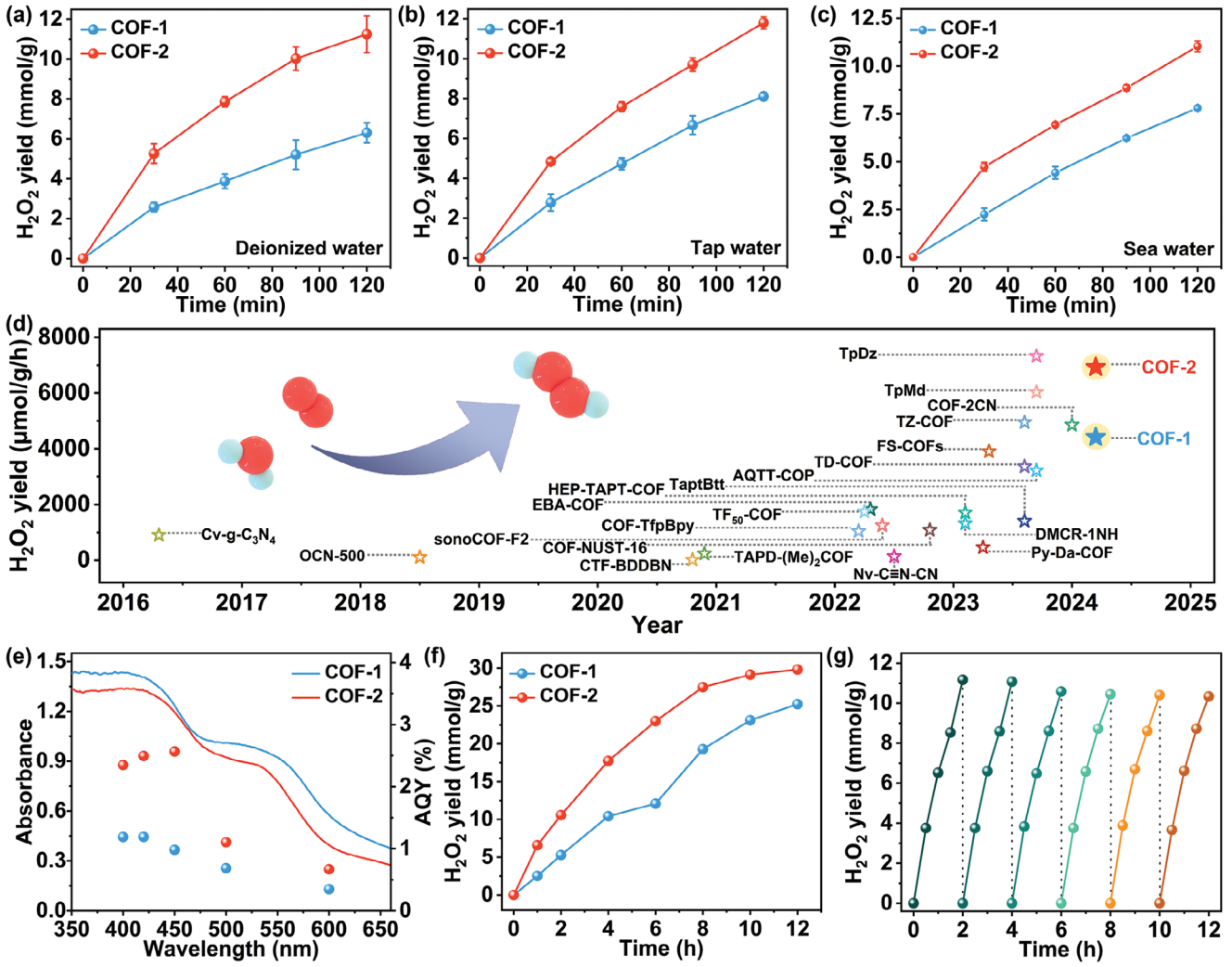

Figure 4. a) Photocatalytic H_2O_2 production performance of COF-1 and COF-2 in deionized water. b) Photocatalytic H_2O_2 production performance of COF-1 and COF-2 in tap water. c) Photocatalytic H_2O_2 production performance of COF-1 and COF-2 in seawater. d) Comparison of photocatalytic H_2O_2 production rates afforded by COF-1 and COF-2 with other recently reported photocatalysts. e) Apparent quantum efficiency (AQY) and electronic absorption spectra of COF-1 and COF-2. f) Long-term photocatalytic H_2O_2 production performance of COF-1 and COF-2 in seawater. g) Photocatalytic H_2O_2 yield over COF-2 for 6-reuse cycles in seawater.

is superior to almost all reported COF photocatalysts under similar conditions, including state-of-the-art COF-F2,[8d] TD-COF[31] and TpMd[15b] (Figure 4d; Table S3, Supporting Information).[23] In addition, photocatalytic H_2O_2 decomposition tests revealed that COF-1 and COF-2 did not decompose H_2O_2 under light irradiation, which was favorable for continuous photocatalytic H_2O_2 generation (Figure S10, Supporting Information). COF-2 exhibits an apparent quantum yield (AQY) of 2.5%, higher than COF-1 (1.2%) at 420 nm (Figure 4e). The solar-to-chemical conversion (SCC) efficiency of COF-1 and COF-2 were calculated to be 0.26% and 0.14% under visible-light irradiation, which is higher than solar-to-biomass efficiency by plants (≈0.1%).[32] Moreover, COF-1 and COF-2 maintained high H_2O_2 production rates during long-term photocatalytic tests in seawater (Figure 4f). In addition, COF-2 maintained good H_2O_2 production performance even after six repeated cycles (Figure 4g). COF-2 further displayed negligible structural change after the photocatalytic H_2O_2 production cycle tests in seawater, evidenced by the FT-IR and PXRD measurements on the used photocatalyst (Figure S11, Supporting Information). To further explore the photocatalytic properties of synthesized COF-2, we conducted photocatalytic uranium extraction studies in ≈1 ppm and ≈20 ppm uranium-spiked tap water and groundwater. As expected, COF-2 demonstrated fast uranium extraction kinetics and delivered a removal efficiency of 97% (in ≈1 ppm spiked tap water) and 92% (in ≈1 ppm spiked groundwater) within 360 min, respectively (Figure S12, Supporting Information). Furthermore, COF-2 can also quickly remove U(VI) from ≈20 ppm spiked tap water and groundwater. According to X-ray photoelectron spectroscopy (XPS) results (Figure S13, Supporting Information), both U(VI) (U $4f_{7/2}$ = 384.1 eV and U $4f_{5/2}$ = 394.8) and U(IV) (U $4f_{7/2}$ = 382.5 eV and U $4f_{5/2}$ = 393.3 eV) species were observed after the photocatalytic tests, indicating that U(VI) and U(IV) coexisted on the surface of COF-2 after the light irradiation. The surface species were likely adsorbed

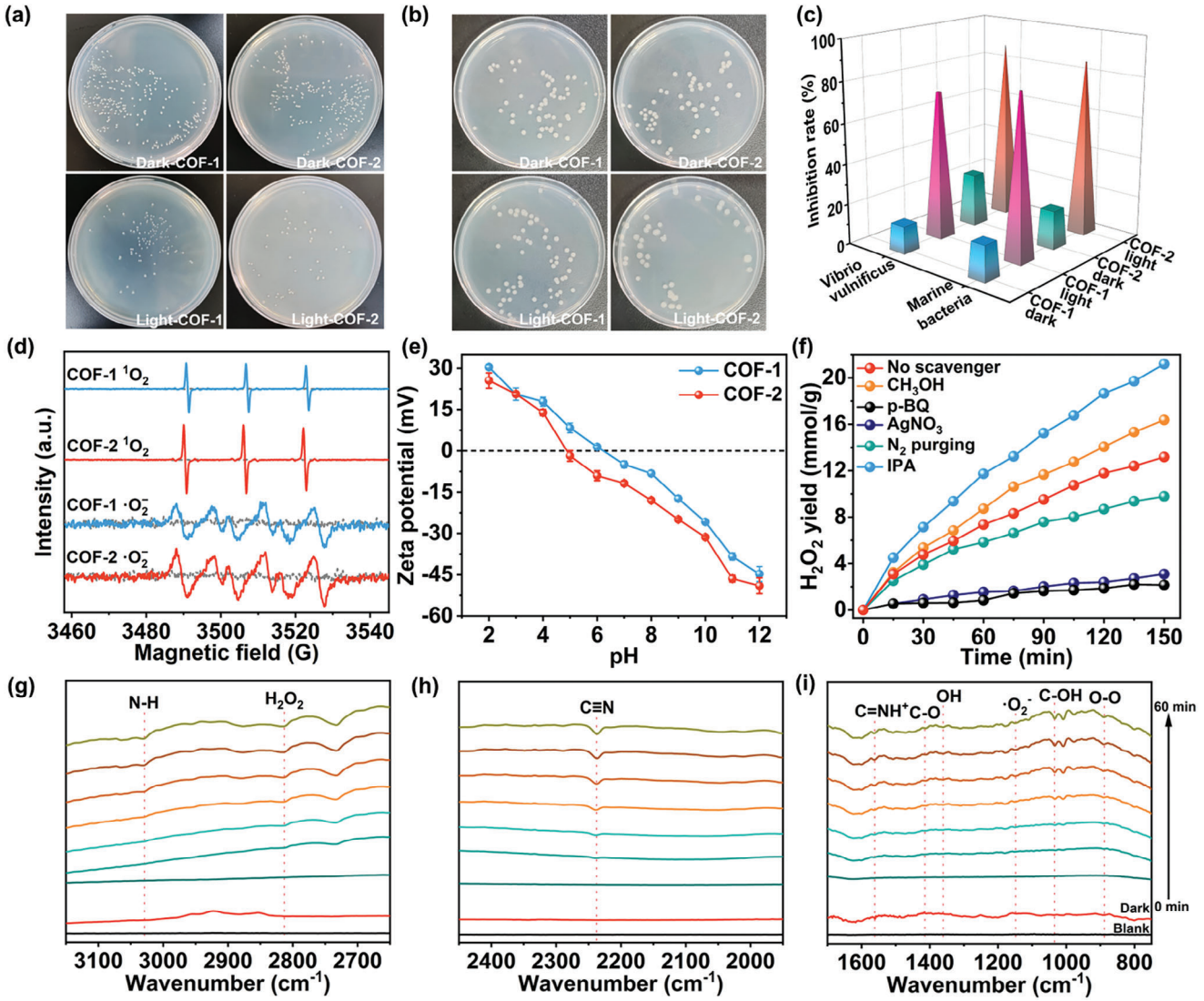

Figure 5. a,b) Photographs of *Vibrio vulnificus* and marine bacteria (mixture) colonies after treatment with COF-1 and COF-2 in the dark and under visible light conditions. c) Summary of anti-biofouling activity of COF-1 and COF-2 under visible light conditions. d) EPR spectra of $^1O_2$-TEMP and $\cdot O_2^-$-DMPO adducts formed by light irradiation of COF-1 and COF-2. e) Zeta potentials of COF-1 and COF-2. f) Quenching experiments for photocatalytic H_2O_2 production. g–i) In situ FT-IR spectra of COF-2 for H_2O_2 photocatalytic processes in the presence O_2.

uranyl (UO_2^{2+}), UO_2, and $(UO_2)O_2{\cdot}2H_2O$.[33] This revealed that the 3D space connected D-A system facilitates energy transfer in photocatalysis, which could be directly used for other applications such as environmental remediation.

Biofouling in seawater can passivate the active sites and prevent light from reaching the photocatalyst, which might seriously affect the H_2O_2 conversion efficiency.[16] Therefore, we evaluated the anti-biofouling properties of COF-1 and COF-2 by testing their inhibition of marine bacteria (mixture) and *Vibrio vulnificus* under dark and visible light irradiation. As shown in **Figure 5**a–c, COF-2 displayed 18.75% and 25.83% inhibition of the marine bacteria(mixture) and *Vibrio vulnificus*, respectively, under dark conditions. When exposed to visible light, the anti-biofouling performance of COF-2 increased dramatically, showing high inhibition rates of 86.04% and 88.45% for marine bacteria(mixture) and *Vibrio vulnificus*, respectively. Compared with COF-2, the anti-biofouling activity of COF-1 was slightly decreased, showing the inhibition rates of 17.19%, 13.25% under dark conditions and 80.52%, 72.44% under visible light irradiation for marine bacteria(mixture) and *Vibrio vulnificus*, respectively.

It is well known that superoxide radicals ($\cdot O_2^-$), singlet oxygen ($^1O_2$), and hydroxyl radicals ($\cdot$OH) produced by photocatalysts can damage the cell walls of marine microorganisms under visible light irradiation.[16] EPR studies were thus carried out to identify the radicals generated during photocatalytic processes in water by COF-1 and COF-2 in the dark and under visible light irradiation conditions (Figure 5d; Figure S14, Supporting Information). No EPR signals were detected under dark conditions for either COF. Conversely, under light irradiation, $\cdot O_2^-$ and $\cdot$OH were generated and trapped using 3,4-dihydro-2,3-dimethyl-2H-pyrrole 1-oxide (DMPO), whilst $^1O_2$ was also detected after adding 2,2,6,6-tetramethylpiperidine (TEMP) as the trapping agent.

The evolution of these reactive oxygen species explained the excellent anti-biofouling activity of the 3D COFs under light irradiation. The photogenerated electron–hole separation in the COFs converted water and oxygen into oxygen-containing radicals under visible light irradiation, which inhibits the growth of marine microorganisms, thus ensuring the efficient photocatalytic production of H_2O_2 in seawater. The tetrazolium (NBT) quantitative experiment shows that the amount of $\cdot O_2^-$ generated by COF-2 was higher than that of COF-1 (Figure S15, Supporting Information), which indicates that the electron transfer efficiency in COF-2 for the production of $\cdot O_2^-$ species is higher than COF-1.

These results revealed that 3D COFs developed in this work, particularly COF-2, offer excellent photocatalytic H_2O_2 production activities and good durability. This may be due to the 3D space connected D-A system and the planar conjugated structure of the naphthyl linker forming a highly extended π-conjugated system in COF-2, promoting the efficiency of electron–hole separation and electronic energy utilization. To obtain a deeper understanding of the relationship between the 3D structural framework and the H_2O_2 production properties, we then carried out a series of experiments and theoretical calculations for COF-1 and COF-2.

2.4. Photocatalytic Mechanism Studies

Zeta potential measurements were used to characterize the surface affinity of COFs for H^+ (Figure 5e). COF-2 has a more negative Zeta potential than COF-1, indicating that COF-2 has a stronger electrostatic attraction toward H^+ which is valuable for the generation of H_2O_2.[18b] To identify the intermediates formed during H_2O_2 production over COF-1 and COF-2 under visible light irradiation, we subsequently performed free radical capture experiments using a range of scavengers, including $AgNO_3$ (for electrons), methanol (for holes), p-benzoquinone (for $\cdot O_2^-$/·OOH), N_2 (for eliminating the presence if O_2) and isopropyl alcohol (Figure 5f).[15b,27] A significant decrease in the H_2O_2 yield for both COFs was observed after purging with N_2 and adding $AgNO_3$, suggesting the production H_2O_2 relied on the reduction of dissolved O_2 by photogenerated electrons, confirming that photocatalytic oxygen reduction reaction (ORR) was the key pathway for photocatalytic of H_2O_2 production in the current work. The H_2O_2 production rates also decreased in the presence of p-benzoquinone, suggesting that $\cdot O_2^-$/·OOH were also involved in a stepped ORR pathway. Methanol caused the opposite trend, which is explained by its strong oxidisability as a hole acceptor (including reaction with ·OH generated via a water oxidation reaction (WOR) pathway). Moreover, the H_2O_2 production rate reached 11.73 mmol g^{-1} h^{-1} by adding 10 vol.% isopropyl alcohol, which is 1.6 times that of the system without the addition of electron donors. These experiments revealed that photogenerated electrons reduce oxygen to $\cdot O_2^-$, which is the rate-controlling step in photocatalytic H_2O_2 production. Subsequently, in situ diffuse reflectance infrared Fourier transform spectroscopy (DRIFTS) measurements was performed on COF-1 and COF-2 to analyze the dynamic changes of the reaction intermediate species (Figure 5g–i; Figure S16, Supporting Information). The DRIFTS spectra showed very weak vibrations over 30 min under dark reaction, indicating that the functional groups of both COF-1 and COF-2 could drive catalysis under dark conditions. Upon light irradiation, a peak at 2815 cm^{-1} emerged corresponded to the O—H stretching vibration of H_2O_2, with the intensity of the peak gradually increasing with photoirradiation time, suggesting that H_2O_2 was being generated on the surface of COFs (Figure 5g–i; Figure S16, Supporting Information).[14b] Signals belonging to N—H (3029 cm^{-1}) and C═NH^+ (1558 cm^{-1}) also showed changes with increasing irradiation time, suggesting the photoinduced imine and carbazole N sites can facilitate H_2O adsorption.[25d] Further, the intensity of C≡N (2231 cm^{-1}) stretching peak also changed with photoirradiation time (Figure 5h; Figure S16, Supporting Information), indicating that the cyano group was part of the active site in the reaction pathway. New signals at 1148 cm^{-1} ($\cdot O_2^-$) and 889 cm^{-1} (O—O stretching) also appeared as the irradiation time increased, indicating that adsorbed O_2 was reduced to $\cdot O_2^-$ by photogenerated electrons.[29] A further peaks at 1360 cm^{-1} also increased in intensity with time, indicating the formation of ·OOH species.[19a,34] The observation of C—O stretching (1413 cm^{-1}) and C—OH stretching (1033 cm^{-1}) peaks were attributed to the formation of surface ·OH species.[17a]

We next performed density functional theory (DFT) and time-dependent DFT (TD-DFT) calculations to better understand the structure-photocatalytic performance relationship of COF-1 and COF-2. In the frameworks of COF-1 and COF-2, the HOMO and LUMO can be isolated on the donor and acceptor segments, respectively (**Figure 6**a,b). The LUMO is distributed on the diphenyl over the dicyanobenzene subunits in both COFs, while the HOMO is located on the carbazolyl moieties, but part of the HOMO of COF-2 is also scattered on the π-conjugate naphthalene linker. These spatially separated molecular orbitals can facilitate efficient intramolecular charge transfer.[35] The calculated VB and CB energies of the COF fragment show that the potential of COF-2 (−2.242 eV) was more positive than that of COF-1 (−2.567 eV). The delocalized HOMO that extends over the entire naphthalene plane in COF-2 can better transfer charge and energy, thereby improving photocatalytic performance. The density of states calculations shows that C and N atoms are mainly involved in the HOMO of both COFs (Figure 6c). The partial density of states (PDOS) of C and N orbitals indicate that the bandgap of COF-2 was narrowed by 0.31 eV compared with the COF-1 counterpart, suggesting more excited electrons could be concentrated upon the electron acceptor unit in COF-2, which is conducive to efficient charge transfer and light utilization. In addition, TD-DFT calculation results of excited state and electron–hole distribution show that the electrons of COF-1 and COF-2 are mainly distributed on dicocyanobenzene, and the holes are distributed along the carbazole junction, which indicates that the photogenerated electrons can be transferred along the D-A pathways after excitation (Figure 6d,e). The energy levels of S_1 and T_1 of COF-1 are 1.669 and 1.661 eV, respectively, while for COF-2 the corresponding values are 1.400 and 1.400 eV, respectively (Figure S17, Tables S4 and S5, Supporting Information). The data indicates that COF-2 is more likely to excite electrons to S_1 after absorbing light, with the narrower energy level gap (ΔE_{ST}) in COF-2 allowing electrons to easily transition from S_1 to T_1 through ISC, thus catalyzing the photocatalytic reaction (Figure S17, Tables S4 and S5, Supporting Information).[36]

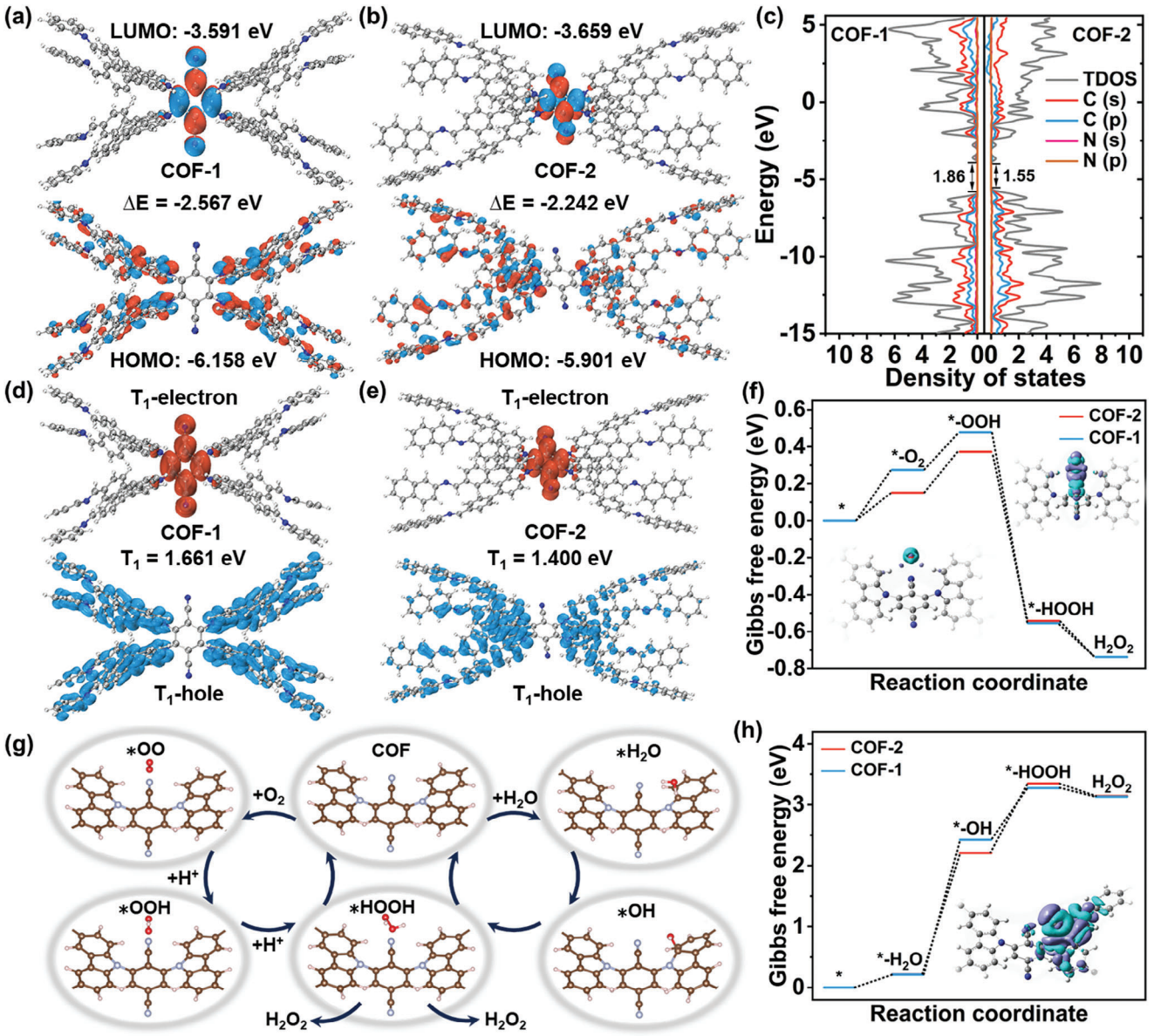

Figure 6. a,b) Calculated HOMO and LUMO distribution of COF-1 and COF-2. c) Total (TDOS) and partial density of states (PDOS) for COF-1 and COF-2. d,e) The T_1 excited state electronic structures of COF-1 and COF-2. f) Calculated energy of COF-1 and COF-2 for reduction of oxygen into H_2O_2 (inset: Charge difference density between $*O_2$, *OOH and adsorption sites on COF-2.). g) The reaction pathway for H_2O_2 production by COFs. h) Calculated energy of COF-1 and COF-2 for oxidation of water into H_2O_2 (inset: Charge difference density between *OH and adsorption sites on COF-2.).

On the basis of the above experimental and theoretical calculations, we summarized the probable mechanism for photocatalytic H_2O_2 production by COF-1 and COF-2. We established that the 4CzTFPN linker in both COFs served as the active site, which could complete the reduction of O_2 to H_2O_2 and the oxidation of H_2O to H_2O_2. In the oxygen reduction pathway, oxygen is first adsorbed onto the dicyanobenzene group and reduced with protonation to form *OOH (Figure 6f,g). Charge difference density maps also reveal this pathway (Figure 6f). The Gibbs free energies (ΔG) of O_2 adsorption ($*O_2$) are 0.27 and 0.15 eV for COF-1 and COF-2, respectively, indicating O_2 adsorption proceeded more readily on COF-2. The rate-determining steps ($*O_2 + H^+ + e^- \rightarrow$ *OOH) for COF-1 exhibited a high energy barrier of 0.48 eV, compared with 0.37 eV for COF-2 in the overall ORR pathway. Afterward, those of the subsequent steps involving the reaction of *OOH with one electron and one H^+ to generate *HOOH, followed by the desorption of H_2O_2, have similar energy barriers on both COF-1 and COF-2. In the water oxidation reaction pathway, the H_2O molecule is adsorbed on a carbazole site, then dehydrogenated to *OH. COF-2 exhibits a smaller ΔG value (2.20 eV) compared to COF-1 (ΔG = 2.42 eV), whilst the energy barrier of COF-2 is close to that of COF-1 for the subsequent conversion of *OH to *HOOH, which then desorbs to give H_2O_2 (Figure 6g,h). Notably, the charge density difference between the pivotal

intermediate *OH and active site near carbazolyl, together with charge redistribution of carbazole unit interacting with *OH, determines the selective formation of *OH at the active site through a stereoscopic donor–acceptor mechanism. These results indicate that H_2O_2 generation is more energetically favorable on the surface of COF-2.

Taken together, the 3D COFs described herein demonstrated excellent photocatalytic H_2O_2 production performance. The excellent photocatalytic activity of these photocatalysts can be attributed to: 1) 3D framework and porosity which allowed for effective mass transport and facilitated easy access of O_2 and H_2O molecules to the catalytic active sites. 2) The 3D space connected D-A system allowed the transferring of electrons through high connectivity of the 3D frameworks, reducing the energy loss for S_0 to S_n transitions and minimizing ΔE_{ST} for efficient ISC, thus improving the photocatalytic energy utilization efficiency. 3) The conjugates structure of the naphthalene linker promotes charge transfer between the donor–acceptor, which is conducive to photogenerated electron–hole separation, boosting photocatalytic H_2O_2 production activity. 4) Excellent resistance to marine biofouling makes the COFs durable under visible light.

3. Conclusion

In summary, we have designed and successfully synthesized two 3D COF photocatalysts, which possess [8+2] connectivity and a bcu topology. Benefiting from the 3D space donor–acceptor system that aided transfer of electrons through the 3D frameworks, both COF-1 and COF-2 showed excellent activity for photocatalytic H_2O_2 production in natural seawater. The conjugated structure of the naphthalene linker in COF-2 enhanced the charge transfer ability of the framework, dramatically promoting the photoactive activity. COF-2 shows excellent photocatalytic performance for H_2O_2 production in natural seawater, which is superior to most of the top-performing COF photocatalysts. This work offers new vistas for the design of robust 3D COFs for photocatalytic H_2O_2 production and other applications.

Supporting Information

Supporting Information is available from the Wiley Online Library or from the author.

Acknowledgements

The authors gratefully acknowledge funding support from the National Science Foundation of China (Grants 22322603; U2167218; 22341602; U2341289) the Beijing Outstanding Young Scientist Program (H.Y., Z.C., X.W.), and the Robert A. Welch Foundation (B-0027) (S.M.). G.I.N.W. is supported by a James Cook Research Fellowship from New Zealand Government funding, administered by the Royal Society Te Apārangi. The authors also thank the Shiyanjia Lab (https://www.shiyanjia.com) for expert assistance with the DFT calculations.

Conflict of Interest

The authors declare no conflict of interest.

Data Availability Statement

The data that support the findings of this study are available from the corresponding author upon reasonable request.

Keywords

covalent organic frameworks, donor–acceptor, hydrogen peroxide, photocatalysis, triplet energy transfer

Received: June 24, 2024
Revised: August 8, 2024
Published online:

[1] a) C. S. Diercks, O. M. Yaghi, *Science* **2017**, *355*, eaal1585; b) K. Geng, T. He, R. Liu, S. Dalapati, K. T. Tan, Z. Li, S. Tao, Y. Gong, Q. Jiang, D. Jiang, *Chem. Rev.* **2020**, *120*, 8814.
[2] F. Jin, T. Wang, H. Zheng, E. Lin, Y. Zheng, L. Hao, T. Wang, Y. Chen, P. Cheng, K. Yu, Z. Zhang, *J. Am. Chem. Soc.* **2023**, *145*, 6507.
[3] L. Ascherl, E. W. Evans, J. Gorman, S. Orsborne, D. Bessinger, T. Bein, R. H. Friend, F. Auras, *J. Am. Chem. Soc.* **2019**, *141*, 15693.
[4] C. Yuan, S. Fu, X. Kang, C. Cheng, C. Jiang, Y. Liu, Y. Cui, *J. Am. Chem. Soc.* **2023**, *146*, 635.
[5] M. Yuan, F. Ma, L. Chen, B. Li, X. Dai, J. Shu, L. He, J. Chen, S. Lin, G. Xie, Z. Chai, S. Wang, *J. Am. Chem. Soc.* **2024**, *146*, 1250.
[6] Z. Yang, J. Liu, Y. Li, G. Zhang, G. Xing, L. Chen, *Angew. Chem., Int. Ed.* **2021**, *60*, 20754.
[7] a) S. Y. Ding, M. Dong, Y. W. Wang, Y. T. Chen, H. Z. Wang, C. Y. Su, W. Wang, *J. Am. Chem. Soc.* **2016**, *138*, 3031; b) M. Hao, Y. Xie, M. Lei, X. Liu, Z. Chen, H. Yang, G. I. N. Waterhouse, S. Ma, X. Wang, *J. Am. Chem. Soc.* **2024**, *146*, 1904.
[8] a) C. J. Wu, X. Y. Li, T. R. Li, M. Z. Shao, L. J. Niu, X. F. Lu, J. L. Kan, Y. Geng, Y. B. Dong, *J. Am. Chem. Soc.* **2022**, *144*, 18750; b) C. Krishnaraj, H. Sekhar Jena, L. Bourda, A. Laemont, P. Pachfule, J. Roeser, C. V. Chandran, S. Borgmans, S. M. J. Rogge, K. Leus, C. V. Stevens, J. A. Martens, V. Van Speybroeck, E. Breynaert, A. Thomas, P. Van Der Voort, *J. Am. Chem. Soc.* **2020**, *142*, 20107; c) W. Zhang, L. Chen, S. Dai, C. Zhao, C. Ma, L. Wei, M. Zhu, S. Y. Chong, H. Yang, L. Liu, Y. Bai, M. Yu, Y. Xu, X. W. Zhu, Q. Zhu, S. An, R. S. Sprick, M. A. Little, X. Wu, S. Jiang, Y. Wu, Y. B. Zhang, H. Tian, W. H. Zhu, A. I. Cooper, *Nature* **2022**, *604*, 72; d) W. Zhao, P. Yan, B. Li, M. Bahri, L. Liu, X. Zhou, R. Clowes, N. D. Browning, Y. Wu, J. W. Ward, A. I. Cooper, *J. Am. Chem. Soc.* **2022**, *144*, 9902; e) L. Grunenberg, G. Savasci, M. W. Terban, V. Duppel, I. Moudrakovski, M. Etter, R. E. Dinnebier, C. Ochsenfeld, B. V. Lotsch, *J. Am. Chem. Soc.* **2021**, *143*, 3430; f) S. Li, R. Ma, S. Xu, T. Zheng, G. Fu, Y. Wu, Z. Liao, Y. Kuang, Y. Hou, D. Wang, P. S. Petkov, K. Simeonova, X. Feng, L. Z. Wu, X. B. Li, T. Zhang, *J. Am. Chem. Soc.* **2022**, *144*, 13953; g) P. Pachfule, A. Acharjya, J. Roeser, T. Langenhahn, M. Schwarze, R. Schomacker, A. Thomas, J. Schmidt, *J. Am. Chem. Soc.* **2018**, *140*, 1423; h) S. Ghosh, A. Nakada, M. A. Springer, T. Kawaguchi, K. Suzuki, H. Kaji, I. Baburin, A. Kuc, T. Heine, H. Suzuki, R. Abe, S. Seki, *J. Am. Chem. Soc.* **2020**, *142*, 9752; i) W. Chen, L. Wang, D. Mo, F. He, Z. Wen, X. Wu, H. Xu, L. Chen, *Angew. Chem., Int. Ed.* **2020**, *59*, 16902; j) D. Chen, W. Chen, Y. Wu, L. Wang, X. Wu, H. Xu, L. Chen, *Angew. Chem., Int. Ed.* **2023**, *62*, e202217479.
[9] Z. Li, T. Deng, S. Ma, Z. Zhang, G. Wu, J. Wang, Q. Li, H. Xia, S. W. Yang, X. Liu, *J. Am. Chem. Soc.* **2023**, *145*, 8364.
[10] a) Z. Chen, J. Wang, M. Hao, Y. Xie, X. Liu, H. Yang, G. I. N. Waterhouse, X. Wang, S. Ma, *Nat. Commun.* **2023**, *14*, 1106; b) M. A. Bryden, E. Zysman-Colman, *Chem. Soc. Rev.* **2021**, *50*, 7587.

[11] a) H. Uoyama, K. Goushi, K. Shizu, H. Nomura, C. Adachi, *Nature* **2012**, *492*, 234; b) J.-X. Wang, L. Gutiérrez-Arzaluz, X. Wang, T. He, Y. Zhang, M. Eddaoudi, O. M. Bakr, O. F. Mohammed, *Nat. Photonics* **2022**, *16*, 869.
[12] S.-S. Zhu, Y. Liu, X.-L. Chen, L.-B. Qu, B. Yu, *ACS Catal.* **2021**, *12*, 126.
[13] a) A. Jati, K. Dey, M. Nurhuda, M. A. Addicoat, R. Banerjee, B. Maji, *J. Am. Chem. Soc.* **2022**, *144*, 7822; b) Q. Zhi, W. Liu, R. Jiang, X. Zhan, Y. Jin, X. Chen, X. Yang, K. Wang, W. Cao, D. Qi, J. Jiang, *J. Am. Chem. Soc.* **2022**, *144*, 21328; c) R. Chen, Y. Wang, Y. Ma, A. Mal, X. Y. Gao, L. Gao, L. Qiao, X. B. Li, L. Z. Wu, C. Wang, *Nat. Commun.* **2021**, *12*, 1354.
[14] a) S. Jin, M. Supur, M. Addicoat, K. Furukawa, L. Chen, T. Nakamura, S. Fukuzumi, S. Irle, D. Jiang, *J. Am. Chem. Soc.* **2015**, *137*, 7817; b) R. Liu, Y. Chen, H. Yu, M. Položij, Y. Guo, T. C. Sum, T. Heine, D. Jiang, *Nat. Catalysis* **2024**, *7*, 195.
[15] a) S. Yang, H. Lv, H. Zhong, D. Yuan, X. Wang, R. Wang, *Angew. Chem., Int. Ed.* **2022**, *61*, e202115655; b) Q. Liao, Q. Sun, H. Xu, Y. Wang, Y. Xu, Z. Li, J. Hu, D. Wang, H. Li, K. Xi, *Angew. Chem., Int. Ed.* **2023**, *62*, 202310556.
[16] H. Yang, M. J. Hao, Y. H. Xie, X. L. Liu, Y. F. Liu, Z. S. Chen, X. K. Wang, G. I. N. Waterhouse, S. Q. Ma, *Angew. Chem., Int. Ed.* **2023**, *62*, 202303129.
[17] a) J. N. Chang, Q. Li, J. W. Shi, M. Zhang, L. Zhang, S. Li, Y. Chen, S. L. Li, Y. Q. Lan, *Angew. Chem., Int. Ed.* **2023**, *62*, e202218868; b) M.-Y. Yang, S.-B. Zhang, M. Zhang, Z.-H. Li, Y.-F. Liu, X. Liao, M. Lu, S.-L. Li, Y.-Q. Lan, *J. Am. Chem. Soc.* **2024**, *146*, 3396.
[18] a) M. Traxler, S. Gisbertz, P. Pachfule, J. Schmidt, J. Roeser, S. Reischauer, J. Rabeah, B. Pieber, A. Thomas, *Angew. Chem., Int. Ed.* **2022**, *61*, e202117738; b) Y. Mou, X. Wu, C. Qin, J. Chen, Y. Zhao, L. Jiang, C. Zhang, X. Yuan, E. Huixiang Ang, H. Wang, *Angew. Chem., Int. Ed.* **2023**, *62*, e202309480; c) W. Weng, J. Guo, *Nat. Commun.* **2022**, *13*, 5768.
[19] a) X. Wang, Y. Jin, N. Li, H. Zhang, X. Liu, X. Yang, H. Pan, T. Wang, K. Wang, D. Qi, J. Jiang, *Angew. Chem., Int. Ed.* **2024**, *63*, 202401014; b) P. Dong, X. Xu, R. Luo, S. Yuan, J. Zhou, J. Lei, *J. Am. Chem. Soc.* **2023**, *145*, 15473; c) T. Y. Yu, Q. Niu, Y. Chen, M. Lu, M. Zhang, J. W. Shi, J. Liu, Y. Yan, S. L. Li, Y. Q. Lan, *J. Am. Chem. Soc.* **2023**, *145*, 8860.
[20] a) X. Xu, P. Cai, H. Chen, H. C. Zhou, N. Huang, *J. Am. Chem. Soc.* **2022**, *144*, 18511; b) F. Jin, E. Lin, T. Wang, D. Yan, Y. Yang, Y. Chen, P. Cheng, Z. Zhang, *Chem* **2022**, *8*, 3064.
[21] E. Jung, H. Shin, B.-H. Lee, V. Efremov, S. Lee, H. S. Lee, J. Kim, W. Hooch Antink, S. Park, K.-S. Lee, S.-P. Cho, J. S. Yoo, Y.-E. Sung, T. Hyeon, *Nat. Mater.* **2020**, *19*, 436.
[22] Y. Zhang, C. Pan, G. Bian, J. Xu, Y. Dong, Y. Zhang, Y. Lou, W. Liu, Y. Zhu, *Nat. Energy* **2023**, *8*, 361.
[23] Y. Sun, L. Han, P. Strasser, *Chem. Soc. Rev.* **2020**, *49*, 6605.
[24] P. Das, G. Chakraborty, J. Roeser, S. Vogl, J. Rabeah, A. Thomas, *J. Am. Chem. Soc.* **2023**, *145*, 2975.
[25] a) P. Li, F. Ge, Y. Yang, T. Wang, X. Zhang, K. Zhang, J. Shen, *Angew. Chem., Int. Ed.* **2024**, *63*, e202319885; b) F. Tan, Y. Zheng, Z. Zhou, H. Wang, X. Dong, J. Yang, Z. Ou, H. Qi, W. Liu, Z. Zheng, X. Chen, *CCS Chem.* **2022**, *4*, 3751; c) X. Liu, R. Qi, S. Li, W. Liu, Y. Yu, J. Wang, S. Wu, K. Ding, Y. Yu, *J. Am. Chem. Soc.* **2022**, *144*, 23396; d) M. Kou, Y. Wang, Y. Xu, L. Ye, Y. Huang, B. Jia, H. Li, J. Ren, Y. Deng, J. Chen, Y. Zhou, K. Lei, L. Wang, W. Liu, H. Huang, T. Ma, *Angew. Chem., Int. Ed.* **2022**, *61*, e202200413; e) J. Sun, H. Sekhar Jena, C. Krishnaraj, K. Singh Rawat, S. Abednatanzi, J. Chakraborty, A. Laemont, W. Liu, H. Chen, Y.-Y. Liu, K. Leus, H. Vrielinck, V. Van Speybroeck, P. Van Der Voort, *Angew. Chem., Int. Ed.* **2023**, *62*, e202216719.
[26] Z. Shan, M. Wu, D. Zhu, X. Wu, K. Zhang, R. Verduzco, G. Zhang, *J. Am. Chem. Soc.* **2022**, *144*, 5728.
[27] Y. Hou, P. Zhou, F. Liu, Y. Lu, H. Tan, Z. Li, M. Tong, J. Ni, *Angew. Chem., Int. Ed.* **2023**, *62*, e202318562.
[28] Z. Teng, Q. Zhang, H. Yang, K. Kato, W. Yang, Y.-R. Lu, S. Liu, C. Wang, A. Yamakata, C. Su, B. Liu, T. Ohno, *Nat. Catal.* **2021**, *4*, 374.
[29] F. Hao, C. Yang, X. Lv, F. Chen, S. Wang, G. Zheng, Q. Han, *Angew. Chem., Int. Ed.* **2023**, *62*, e202315456.
[30] C. Qin, X. Wu, L. Tang, X. Chen, M. Li, Y. Mou, B. Su, S. Wang, C. Feng, J. Liu, X. Yuan, Y. Zhao, H. Wang, *Nat. Commun.* **2023**, *14*, 5238.
[31] J.-Y. Yue, L.-P. Song, Y.-F. Fan, Z.-X. Pan, P. Yang, Y. Ma, Q. Xu, B. Tang, *Angew. Chem., Int. Ed.* **2023**, *62*, e202309624.
[32] L. Chen, L. Wang, Y. Wan, Y. Zhang, Z. Qi, X. Wu, H. Xu, *Adv. Mater.* **2020**, *32*, 1904433.
[33] a) G. Lu, A. J. Haes, T. Z. Forbes, *Coord. Chem. Rev.* **2018**, *374*, 314; b) H. Zhang, W. Liu, A. Li, D. Zhang, X. Li, F. Zhai, L. Chen, L. Chen, Y. Wang, S. Wang, *Angew. Chem., Int. Ed.* **2019**, *58*, 16110.
[34] Y. Luo, B. Zhang, C. Liu, D. Xia, X. Ou, Y. Cai, Y. Zhou, J. Jiang, B. Han, *Angew. Chem., Int. Ed.* **2023**, *62*, e202305355.
[35] H. Yang, S.-K. Peng, J. Zheng, D. Luo, M. Xie, Y.-L. Huang, X. Cai, J. Wang, X.-P. Zhou, D. Li, *Angew. Chem., Int. Ed.* **2023**, *62*, e202310495.
[36] R. Hojo, K. Bergmann, S. A. Elgadi, D. M. Mayder, M. A. Emmanuel, M. S. Oderinde, Z. M. Hudson, *J. Am. Chem. Soc.* **2023**, *145*, 18366.